Biophysical Journal
Article

Biophysical Society

Micromechanical Analysis of the Hyaluronan-Rich Matrix Surrounding the Oocyte Reveals a Uniquely Soft and Elastic Composition

Xinyue Chen,[1,2] Rita Bonfiglio,[3] Suneale Banerji,[4] David G. Jackson,[4] Antonietta Salustri,[3] and Ralf P. Richter[1,2,5,*]

[1]CIC biomaGUNE, San Sebastian, Spain; [2]Max Planck Institute for Intelligent Systems, Stuttgart, Germany; [3]Department of Biomedicine and Prevention, Faculty of Medicine, University of Rome Tor Vergata, Rome, Italy; [4]MRC Human Immunology Unit, Weatherall Institute of Molecular Medicine, University of Oxford, Oxford, United Kingdom; and [5]Laboratory of Interdisciplinary Physics, University Grenoble Alpes-CNRS, Grenoble, France

ABSTRACT The cumulus cell-oocyte complex (COC) matrix is an extended coat that forms around the oocyte a few hours before ovulation and plays vital roles in oocyte biology. Here, we analyzed the micromechanical response of mouse COC matrix by colloidal-probe atomic force microscopy. We found that the COC matrix is elastic insofar as it does not flow and its original shape is restored after force release. At the same time, the COC matrix is extremely soft. Specifically, the most compliant parts of in vivo and in vitro expanded COC matrices yielded Young's modulus values of 0.5 $\pm$ 0.1 Pa and 1.6 $\pm$ 0.3 Pa, respectively, suggesting both high porosity and a large mesh size ($\geq$100 nm). In addition, the elastic modulus increased progressively with indentation. Furthermore, using optical microscopy to correlate these mechanical properties with ultrastructure, we discovered that the COC is surrounded by a thick matrix shell that is essentially devoid of cumulus cells and is enhanced upon COC expansion in vivo. We propose that the pronounced nonlinear elastic behavior of the COC matrix is a consequence of structural heterogeneity and serves important functions in biological processes such as oocyte transport in the oviduct and sperm penetration.

INTRODUCTION

Cumulus cells are a distinct population of somatic cells surrounding the oocyte in mature ovarian follicles (1). In response to the hormone surge that ultimately triggers ovulation, they produce a unique oocyte-embedding matrix. This process, known as cumulus expansion, involves the rapid synthesis of hyaluronan (HA) (2), a polysaccharide of the glycosaminoglycan family, and in concert, the cross-linking of HA polymers with a complex of several distinct proteins and proteoglycans (3–8). The resulting matrix, termed the cumulus cell-oocyte complex (COC) matrix, contains not only the oocyte but also a large number of cumulus cells, and is essential for successful ovulation and in vivo fertilization. In particular, the COC matrix has been proposed to modulate cumulus cell and sperm intracellular signaling (1), and it is known to facilitate the transport of COCs along the oviduct (9) and to play important roles in the attraction (4,10), capacitation (11), and selection (12) of sperm. Consequently, for many years, the quality of cumulus expansion has been a criterion for selecting oocytes for in vitro fertilization (13). Intact COCs can also be isolated from the follicle and stimulated to synthesize HA-rich matrix during in vitro maturation of mammalian oocytes. Although the in vitro synthesized matrix is apparently similar to that formed in vivo, it has been suggested that it could be deficient in some components that are provided within the ovarian follicle by neighboring cells, thereby establishing a different microenvironment for the oocyte (1).

It is now well established that the mechanical properties of the extracellular matrix (ECM) have profound effects on the cells that they surround, and critically affect basic cellular processes such as proliferation, motility (14), and differentiation (15), in addition to pathologies such as tumor progression (16). Thus, it is reasonable to hypothesize that the mechanical properties of the COC matrix also contribute to the control of oocyte behavior. The functional importance of COC matrix softness was strikingly illustrated, for example, in videos of oocyte pickup by the mammalian oviduct, where a perturbed and stiffened matrix was found to impair transport (17). Moreover, the mechanical properties

Submitted January 4, 2016, and accepted for publication March 21, 2016.

*Correspondence: rrichter@cicbiomagune.es

Editor: Jennifer Curtis.

http://dx.doi.org/10.1016/j.bpj.2016.03.023

of the ECM are ultimately determined by the properties of the constituent molecules and their interactions. The salient morphological features of the COC matrix are extreme hydration, a highly dynamic nature, and a low degree of order, all of which make it difficult to study the ultrastructure of the COC matrix directly by using conventional methods such as optical and electron microscopy. In this regard, a characterization of the mechanical properties of the COC matrix could indirectly provide valuable information about its morphology and ultrastructure. Currently, however, only very limited information about the mechanical properties of the COC matrix is available. Although its elasticity has been documented on the basis of a macroscopic stretching assay (18) and an oviduct transport assay (19) developed many years ago, we still lack knowledge about the local mechanical properties and the mechanical heterogeneity of the COC matrix.

Several methods to probe the local mechanical properties of tissues, the ECM, and cells have emerged over the last two decades, including particle-tracking microrheology (20,21), optical force probe microscopy (22), and atomic force microscopy (AFM) (23–28). The ability to probe a large range of magnitudes in elastic modulus (from pascals to gigapascals (29,30)) and length scales (from nanometers to micrometers (23,25)) makes AFM particularly versatile (31). In colloidal-probe AFM, this is achieved by using hard spheres of the desired size as indentation probes attached to AFM cantilevers of the appropriate softness.

In this study, we analyze the micromechanical response of mouse COC matrix using colloidal-probe AFM. We identify the COC matrix as a biological material that displays a unique combination of elasticity and extreme softness. Second, using quantitative compressibility analysis, we reveal the COC matrix to be mechanically heterogeneous. Finally, by combining AFM with optical microscopy, we show that this unusual heterogeneity stems from an additional and previously undescribed thick outer matrix layer that is completely devoid of cumulus cells. We discuss the implications of our findings for the nanoscale morphology and potential biological functions of the COC matrix.

MATERIALS AND METHODS

Materials

Oligo-ethylene glycol (OEG) was prepared as a solution comprising a 1 mM mixture of OEG thiol (386.5 Da) and biotinylated OEG thiol (788 Da; both from Polypure, Oslo, Norway) at a molar ratio of 99:1 in synthesis grade ethanol, and stored in the dark at 4°C. Lyophilized streptavidin (SAv; Sigma-Aldrich, St. Louis, MO) was dissolved in ultrapure water and stored as aliquots at a concentration of 1 mg/mL at −20°C. Lyophilized bovine serum albumin (BSA; Sigma-Aldrich) was freshly dissolved in ultrapure water and used at a concentration of 10 mg/mL for all passivation purposes.

A sample preparation buffer comprising 10 mM HEPES and 150 mM NaCl at pH 7.4 was used for the preparation of COC-capturing substrates. Throughout the AFM measurements, COCs were maintained in culture medium consisting of minimum essential medium with Earle's salts, buffered at pH 7.3 with 20 mM HEPES and supplemented with 50 μg/mL gentamycin, 0.3 mM sodium pyruvate, 1 mg/mL BSA, and 1 mM 8-bromoadenosine 3′,5′-cyclic monophosphate (8-Br-cAMP), a membrane-permeable cyclic AMP analog that stabilizes the expanded cumulus matrix (32).

Polystyrene microspheres (91.0 ± 1.3 μm diameter; Polysciences, Eppelheim, Germany) were washed first in ethanol and then in ultrapure water (five times each), dried in a vacuum oven at 40°C for 3 h, and stored at 4°C.

Cloning and purification of biotinylated and soluble CD44

The full CD44 ectodomain sequence terminating at proline 267 was amplified from human CD44S cDNA using the high-fidelity polymerase pfu Ultra AD (Agilent) together with the forward primer hCD44-14 BamHI F 5′ GCGGGATCCGAAGGGGTAGGCACGA TGGCCAGG and the reverse primer hCD44 801 10H* XhoI R 5′GCGCCTCGAG*TTA*GTG ATGGTG ATGGTGATGGTGATGGTGATGCCACTCGATTTTCTGTGCCTCGAA GATGTCATTCAGGCCGGATCTAGGAATTTGGGGTGTCCTTATAGG, which encodes a target site for biotin ligase and a 10-histidine (His) tag. The amplified fragment was cloned into a variant of the pHR Sin vector (33) carrying an internal ribosome entry site upstream of a gene encoding emerald GFP and introduced into HEK 293T cells by transfection. Culture supernatants containing virus-like particles were then used to transduce CHO K1 cells together with the lentiviral packaging and envelope plasmids pMD.G and p8.91 using Genejuice (Merck, Darmstadt, Germany), and selected for GFP expression by flow cytometry. Secreted CD44 His-tagged protein was subsequently purified from culture supernatants using a His Trap column (GE Healthcare, Little Chalfont, UK) before biotinylation, using a BirA-500 kit (Avidity, Denver, CO) according to the manufacturer's instructions and removal of free biotin by size-exclusion chromatography. The purified CD44 protein with a C-terminal biotin tag (b-CD44) was stored at 0.5 mg/mL in phosphate-buffered saline at −20°C until it was used for the preparation of COC-capturing substrates.

Preparation of colloidal-probe AFM cantilevers

Tipless V-shaped Si_3N_4 cantilevers with a nominal spring constant of 0.06 N/m (NP-OW; Veeco Probes, Camarillo, CA) were treated for 30 min with UV/ozone (UV/Ozone ProCleaner; Bioforce Nanoscience, Ames, IA). Polystyrene microspheres were dispersed on a cleaned and UV/ozone-treated glass coverslip, and attached to the cantilever using a UV-cured adhesive (NOA 61; Thorlabs, Dachau, Germany). Positioning and attachment were aided by a micromanipulator (Patchstar; Scientifica, Uckfield, UK) and an optical microscope (Axio Observer; Zeiss, Oberkochen, Germany). The real cantilever spring constant was determined to be 0.076 ± 0.004 N/m, using the thermal noise method (34), from an average over three cantilevers with colloidal probes attached. Before use, the colloidal-probe AFM cantilever together with the chip and chip holder was immersed in BSA for 20 min, for surface passivation. Excess BSA was removed by washing with sample preparation buffer.

Preparation of substrates

Glass coverslips (1.5 mm, 24 × 24 mm^2; Menzel Gläser, Braunschweig, Germany) were gently wiped with lint-free tissue (Kimtech Science, Surrey, UK), immersed for 3 h in freshly prepared piranha solution composed of concentrated H_2SO_4 (95–98%; Scharlab, Barcelona, Spain) and H_2O_2 (50%; Scharlab) in a 3:1 volume ratio, thoroughly rinsed with ultrapure water, blow-dried with N_2 gas and stored in sealed petri dishes. For gold (Au) coating, clean glass coverslips underwent 10 min plasma cleaning in the vacuum chamber of a magnetron sputter system (ATC 1800 UHV; AJA

International, Scituate, MA) before deposition of a 0.5 nm adhesive titanium interlayer followed by a 5 nm Au layer. All substrates were UV/ozone treated for 30 min before further use.

To generate COC-capturing substrates, a previously established protocol (35,36) for the orientated immobilization of biotin-tagged molecules was applied. The Au-coated coverslips were first immersed in OEG solution overnight, rinsed with ethanol and ultrapure water, blow-dried with N_2 gas, and attached using a two-component glue (Twinsil; Picodent, Wipperfürth, Germany) to a titanium holder that was custom-designed for operation with a combined AFM/optical microscopy setup. The surface coated with the biotinylated OEG monolayer was then incubated with 20 μg/mL SAv for 30 min, followed by 5 μg/mL b-CD44 for 30 min. Excess proteins in the solution phase were removed by rinsing after each incubation step, and protein-coated surfaces were kept wet throughout the preparation and measurement procedures.

In vivo and in vitro expansion of COCs

In vivo and in vitro expansion of mouse COCs was induced as described previously (2). Briefly, adult female Swiss CD1 mice were primed by intraperitoneal injection of 5 IU pregnant mare serum gonadotropin to promote the formation of multiple antral follicles, and 44–48 h later received a 5 IU intraperitoneal injection of human chorionic gonadotropin to induce COC expansion and ovulation. In vivo expanded COCs were then isolated from oviducts soon after ovulation (14 h from human chorionic gonadotropin injection), transferred with a glass micropipette to tubes in ice containing 100 μL of culture medium, and immediately frozen at -80°C.

To induce in vitro expansion, female mice were sacrificed 44–48 h after injection of pregnant mare serum gonadotropin, and COCs were isolated from the ovaries. Approximately 10 COCs were cultured under oil in a 20 μL drop of culture medium containing 1 mM 8-Br-cAMP and supplemented with 5% fetal calf serum for 15 h at 37°C in 5% CO_2. At the end of culture, in vitro expanded COCs were collected and stored as described above for in vivo expanded COCs.

Immobilization of COCs

COCs were thawed on ice for ~1 h before they were transferred to a COC-capturing substrate. Visual inspection under the microscope revealed that the thawed in vivo expanded COCs were comparable in appearance to those freshly isolated from the oviduct. In particular, the spatial extension of the cumulus cell cloud was not visibly altered by the freeze-thaw cycle and remained virtually unchanged for several hours after thawing. The matrix did not dissociate and the mechanical response of the matrix to gentle stretching with a pair of tweezers also remained comparable, indicating that the freeze-thaw cycle did not affect the matrix morphology appreciably.

For transfer of COCs, 200 μL micropipette tips were modified to enlarge the aperture diameter to ensure COC uptake and release with minimal stress, and passivated with BSA to reduce COC adhesion. The tips were gently manipulated (with monitoring through a phase-contrast microscope) to facilitate isolation of individual oocytes with their cumulus matrix from the original multi-oocyte clusters and their subsequent immobilization at desired positions on the COC-capturing substrate. Care was taken to keep the COCs fully immersed in solution during the immobilization process, and 100 μL of a measurement solution was added after the COCs were immobilized. AFM measurements were performed at room temperature and typically lasted 2–5 h. The immobilized COCs were found to be stable during this time, i.e., the spatial arrangement of the oocyte and the cumulus cells did not change appreciably. Matrix deformation under gentle stretching with tweezers was qualitatively similar at room temperature and at 37°C, suggesting that the mechanical properties do not change appreciably over this temperature range.

Force measurements by colloidal-probe AFM

AFM measurements were performed with a NanoWizard II (JPK Instruments, Berlin, Germany) installed on an optical microscope (Axio Observer; Zeiss). The AFM was equipped with a CellHesion module providing a z-piezo actuation range of 100 μm. The approach speed was 20 μm/s unless stated otherwise. Before each measurement, the cantilever sensitivity was determined from the hard-wall-contact regime of force curves obtained on a cleaned and BSA-passivated glass coverslip in sample preparation buffer. COC-capturing substrates bearing COCs were then mounted and probed in the measurement solution. Reference force curves were acquired at locations devoid of COCs to define the z location of the substrate and to test for contaminants on the colloidal probe. Only probes that showed minimal interactions (i.e., <1 μm interaction range) before hard-wall contact were used for further analysis. Force curves on the COC were acquired at desired positions, with a lateral resolution of a few micrometers (determined by the accuracy of the microscope's manual xy translation stage) and an accuracy in the distance from the glass substrate of ~10 μm (determined from the repeatability in z positioning by the stepper motor of the AFM head). At least three force curves were collected per position.

Data were corrected for linear thermal drifts in the cantilever deflection, and force versus distance curves were computed using established methods (31) implemented in JPK data-processing software. Fits of contact mechanics models (such as the Hertz model; vide infra) to force curves were also performed with the JPK data-processing software, with the measured forces around the contact point $\delta = 0$ averaged and offset to zero.

RESULTS

Immobilization of the COC matrix and experimental setup

The experimental setup used to characterize the local response of COC matrix to compression is schematically shown in Fig. 1 *A*. The AFM cantilever was used with a colloidal probe (i.e., a microsphere) of 90 μm diameter. Such large probes were necessary to provide the required sensitivity for the assays. In initial tests, we noted that the COCs did not adhere efficiently to plain glass or plastic substrates, which is a critical requirement for reproducible AFM measurements. Hence, we prepared a SAv-functionalized substrate that was coated with soluble biotin-tagged ectodomains of the HA receptor CD44 (Fig. 1 *A*, *inset*) to allow more stable tethering via HA in the COC matrix (37). The SAv monolayer thus served as a "molecular breadboard" (36) on which CD44 was immobilized via its carboxyl terminus with its ligand-binding domain arranged in the same orientation as the intact receptor in the cell membrane. As shown in Fig. 1 *B*, when a COC approached the CD44-functionalized substrate, it adhered rapidly and the immobilized COC adopted a stable morphology within a few seconds. This immobilization method worked for COCs expanded in vivo as well as in vitro. We compared these two types of matrix to assess whether the in vitro expansion conditions affected COC matrix mechanics compared with the in vivo scenario. Importantly, COCs did not adhere in the absence of CD44, indicating that the immobilization occurred specifically via HA. Inspection by optical microscopy revealed that cumulus cells in the COC that were located adjacent to the

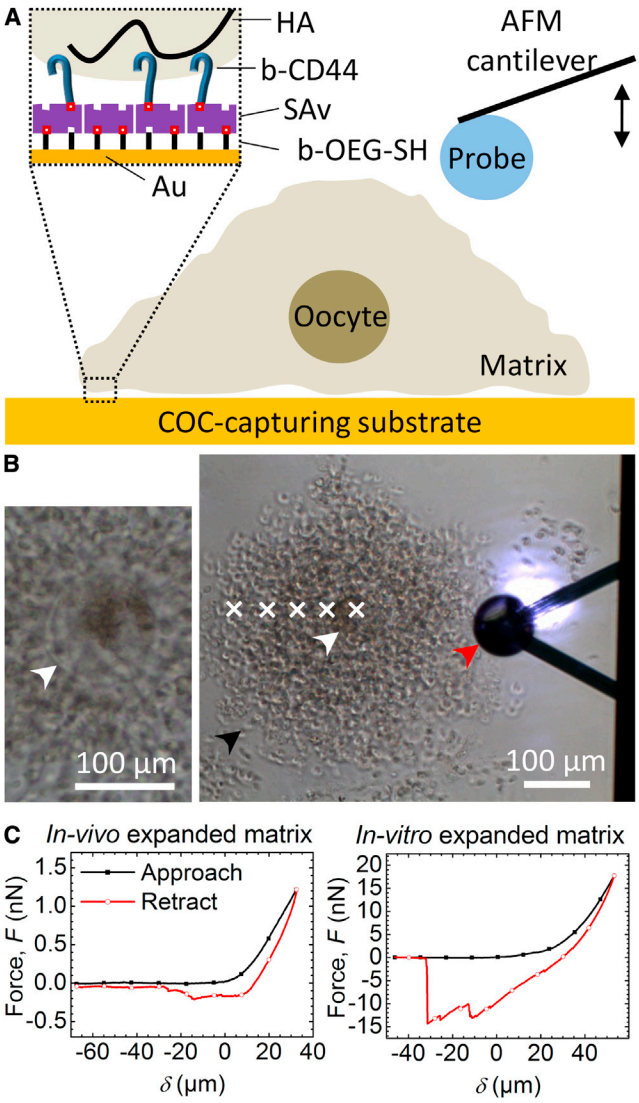

FIGURE 1 (*A*) Scheme of the AFM force-indentation measurement setup. The inset illustrates the assembly of the COC-capturing surface. (*B*) Representative optical micrograph of the measurement setup (*right*). The red arrowhead marks the colloidal probe attached to the V-shaped AFM cantilever and the chip (*right*: the shiny spot on the upper cantilever arm is the laser detecting cantilever deflection). Cumulus cells in the COC matrix (one is marked with a *black arrowhead*) and the oocyte (*white arrowhead*) are also visible. Force curves were acquired at locations labeled with white crosses, starting above the oocyte center and interspaced by 50 μm. The left micrograph provides a magnified view of an oocyte, where the zona pellucida surrounding the oocyte (marked by a *white arrowhead*) can be identified. (*C*) Representative curves of force versus distance from contact point δ, acquired upon approach to (*black line with solid square symbols*) and retraction from (*red line with open circle symbols*) in vivo (*left*) and in vitro (*right*) expanded COC matrices; δ was set to 0 at the contact point at approach, and positive distances correspond to sample indentation.

substrate remained immobile under the influence of gentle pipette-induced flow, indicating firm adhesion of the COC matrix. By comparison, more distantly located cumulus cells were transiently displaced, indicating that the matrix was easily deformed.

Representative force curves obtained upon indentation of in vivo and in vitro expanded COCs at a location on top of the oocyte are shown in Fig. 1 *C*. The approach curve shows an extended baseline where the colloidal probe was not in contact with the sample, followed by a monotonic increase in force reflecting the response of the COC matrix to compression. The length of the baseline was chosen to extend at least 40 μm to enable reliable determination of the contact point ($\delta = 0$), which was operationally defined as the position in the approach curve at which the force exceeded the baseline level by 50 pN. This threshold force was slightly above the instrument noise level.

Attractive features (i.e., negative force) were not observed in the approach curves, but they were always present in the retract curves. This reveals that some residual adhesion between the colloidal probe and the COC occurred despite passivation of the probe with BSA. It also implies that probe-sample adhesion must increase gradually in the course of the indentation process. The magnitude of the adhesion forces varied. In vivo expanded COCs typically showed an adhesion of a few hundred piconewtons, occasionally rising to values in the low-nanonewton range, whereas in vitro expanded COCs displayed values in the range of 5–10 nN, or in some cases only a few hundred piconewtons. The exact shape of the retract curves also varied from one measurement to the next, even on the same spot, and yielded multiple unbinding peaks. This indicates that the detachment of the matrix from the colloidal probe occurs stochastically in steps, and suggests that the COC matrix may be heterogeneous on the scale of the interaction area. Adhesion frequently persisted a few tens of micrometers beyond the contact point (Fig. 1 *C*), indicating that the COC matrix can be stretched significantly. The overall shape and position of the COC matrix were not visibly affected during indentation or stretching with the colloidal AFM probe as observed by optical microscopy. This confirmed that the COC matrix was stably immobilized, thus enabling repeated and controlled indentations at well-defined positions.

COC matrix is an elastic material

To investigate the mechanical response of the COC matrix to applied force, we indented the matrix atop oocytes repeatedly and at various loading rates (Fig. 2). The shapes of approach curves obtained during the first and subsequent indentations at the same position on the COC matrix were virtually identical for COCs expanded in vivo (Fig. 2 *A*) as well as in vitro (Fig. 2 *B*). Moreover, the distances of the contact point from the glass substrate also remained unchanged. This indicates that the matrix fully recovers its original shape when the compressive force is released. In other words, COC deformation is elastic and not plastic.

The force responses of in vivo expanded COC matrices were sensitive to the loading rate. For example, applying a more rapid rate of compression led to a marked increase in

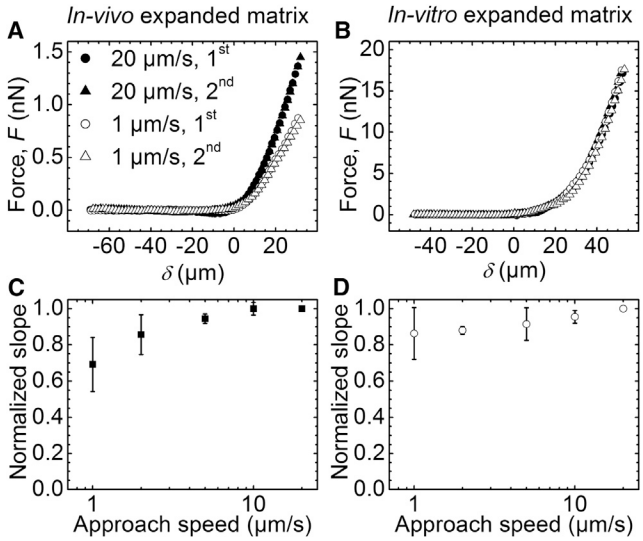

FIGURE 2 Effects of compressive forces on indentation of the COC matrix: elastic versus plastic and viscous deformation. (*A* and *B*) Representative curves of force versus distance from contact point δ, measured on COCs expanded in vivo (*A*) and in vitro (*B*). The first and second approach curves obtained at a previously unperturbed position on the COC are shown for two selected approach speeds (1 μm/s and 20 μm/s, as indicated). (*C* and *D*) Slopes measured between $\delta = 25$ and 30 μm in series of force versus distance curves acquired at fixed positions with varied approach speed, normalized by the slope at 20 μm/s. Data represent the mean $\pm$ standard deviation from measurements on three COCs each, expanded in vivo (*C*) and in vitro (*D*).

the force required to generate a given indentation (Fig. 2 *A*). To analyze this dependence, we computed the slopes of the force versus distance curves at a selected indentation depth ($25\ \mu\text{m} < \delta < 30\ \mu\text{m}$). As shown in Fig. 2 *C*, the value was significantly lower at 1 μm/s (the lowest rate measured) than at 20 μm/s (the highest rate measured). This suggests that there is a viscous component to the mechanical response. Interestingly, a plateau was observed at higher loading rates, indicating a transition from a viscoelastic to a purely elastic behavior at ~5 μm/s. COC matrices expanded in vitro showed no significant loading-rate dependence (Fig. 2 *D*), indicating that this matrix remained purely elastic across the measured range.

Quantification of COC matrix elasticity

The Young's modulus (E) of the COC matrix was determined from force (F) versus indentation ($\delta > 0$) curves using the Hertz indentation model (38):

$$F = \frac{4}{3}\frac{E}{1-\mu^2}\sqrt{R\delta^3}, \qquad (1)$$

where R represents the radius of the spherical probe (45 μm) and μ is Poisson's ratio (39). Most materials have Poisson's ratio values ranging between 0 and 0.5 (40), and we fixed $\mu = 0.5$ for simplicity. This implies that E will be underestimated by at most 25% depending on the exact value of μ. The simplified form of the Hertz model given in Eq. 1 assumes that E is much smaller than the Young's modulus of the probe (in the gigapascal range for polystyrene (30)), and R is much smaller than the effective radius of the probed sample. Both conditions were met in our experiments (vide infra).

The Hertz model provided satisfactory fits when the first 10 μm of indentation were considered for analysis (Fig. 3 *A*, *solid line*). The resulting Young's modulus of matrix expanded in vivo was extremely low: an average from measurements atop the oocyte in three COCs gave $E = 0.5 \pm 0.1$ Pa. The Young's modulus values for in vitro expanded COC matrices were severalfold higher, $E = 1.6 \pm 0.3$ Pa. Extrapolation of the fit (Fig. 3 *A*, *dotted line*), however, revealed that the Hertz model does not adequately describe the experimental data at larger indentations. We considered several effects to explain this discrepancy.

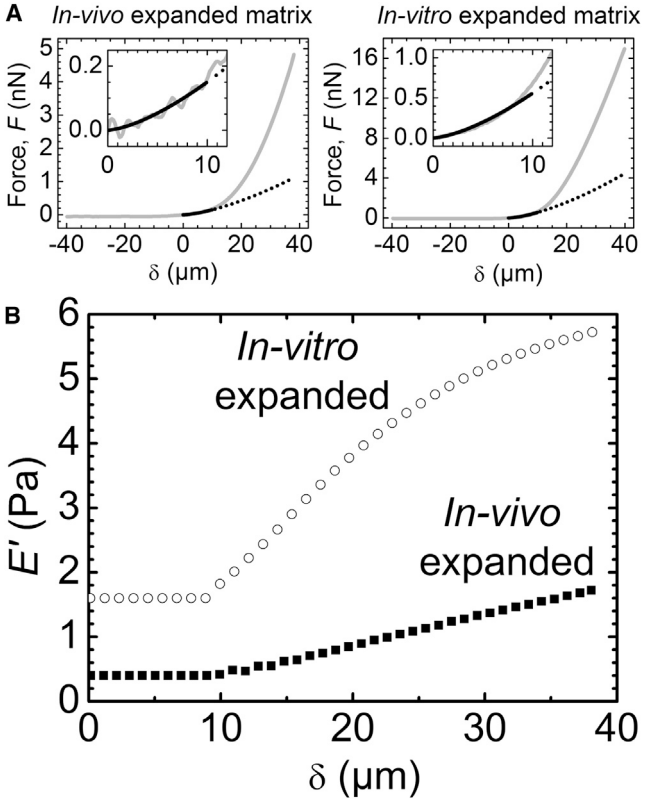

FIGURE 3 Quantification of COC matrix elasticity. (*A*) Representative curves of force versus distance from contact point δ, acquired on top of the oocyte center of in vivo (*left*) and in vitro (*right*) expanded matrix (*gray solid lines*), fitted to the Hertz model over $0 \le \delta \le 10$ μm (*black solid line*) that yields values for Young's modulus of 0.4 and 1.6 Pa, respectively. The black dotted line is an extrapolation of the fit, illustrating that the Hertz model does not reproduce data yielding large indentation values accurately, and that the matrix effectively stiffens upon compression. Data over $0 \le \delta \le 12$ μm are magnified (*insets*) to illustrate the quality of the fits. (*B*) Effective elastic moduli E' for a COC expanded in vivo (*solid squares*) and in vitro (*open circles*). The force curves in (*A*) were downsampled to reduce scatter and then used for analysis. For $0 \le \delta \le 10$ μm, E' was determined through a fit with Eq. 1; for $\delta > 10$ μm, E' was calculated with Eq. 2.

First, the Hertz model requires the indentation depth to be small compared with the sample thickness (38). This was the case in our experiments (vide infra). Second, the maximal indentation depth in our experiment approached the radius of the indenter ($\delta \sim R$), whereas the Hertz model is strictly valid only for $\delta << R$. However, a comparison with an improved model developed by Sneddon (41) shows that the Hertz model overestimates the force at a given indentation and fixed Young's modulus, which is the opposite of what was observed in the experiment (Fig. 3 *A*). Moreover, the discrepancy between the two models remains below 10% for all $\delta < R$ (Fig. S1 in the Supporting Material), implying that the Hertz model provides a reasonable approximation even at the largest measured indentations. Third, the Hertz model assumes zero probe-sample adhesion. The absence of negative forces in the approach curves (Fig. 1 *C*) indicated that adhesion was indeed virtually absent at small indentations in our experiments. The negative forces in the retract curves (Fig. 1 *C*) revealed that adhesion developed gradually upon indentation, and this would affect the shape of the approach curve at larger indentations in a way that is not properly accounted for in the Hertz model. However, since a reduction in the force would be expected, again opposite to what is seen in Fig. 3 *A*, adhesive interactions also cannot explain the discrepancy between the Hertz model and the experiment.

Ultimately, the Hertz model makes the important assumption that the probed material is isotropic and linearly elastic. Thus, the enhanced increase in the compression force with indentation observed in the experiment (Fig. 3 *A*) would indicate that the COC matrix effectively stiffens upon compression. We sought to obtain a more detailed characterization of the matrix mechanical properties as a function of indentation. To this end, we defined the elastic modulus E' by considering only the force F' at a given indentation depth $\delta = \delta' > 0$, but not the shape of the force curve between the contact point ($\delta = 0$) and δ', for the Hertz model analysis. From Eq. 1, we find

$$E' = \frac{3}{4}\left(1-\mu^2\right)\frac{F'}{\sqrt{R\delta'^3}}. \qquad (2)$$

E' provides a simple quantification of matrix elasticity. For small indentations, i.e., in the linear elastic regime where the Hertz model reproduces the experimental data well, it is identical to the Young's modulus E. For large indentations, where the Hertz model deviates from the experimental data ($\delta > 10$ μm in our case), it represents a measure of nonlinear elasticity. We note that the way in which nonlinear effects influence the shape of the force versus distance curves may depend in complex ways on the shape and size of the employed probe, as well as the internal organization of the matrix. In addition, the force curves at large compression are also likely to be affected by probe-sample adhesion (Fig. S2). Therefore, we consider E' to be an effective measure of matrix elasticity in the nonlinear elastic regime.

Fig. 3 *B* shows the result of this analysis on representative force curves acquired in the central region above the oocytes. E' was a few fold higher for in vitro expanded matrix (*open circles*) than for in vivo expanded matrix (*solid squares*) irrespective of the indentation, and increased by a few fold over the accessible indentation range of 40 μm. Nonlinear effects were appreciable and more pronounced for in vitro expanded matrix.

Quantification of COC matrix extension

Because the HA-rich matrix is not directly visible by optical microscopy, the distribution of cumulus cells is commonly used as an indirect measure for COC matrix extension. In our assay, the contact point determined through indentation measurements provided an alternative measure for matrix extension. Interestingly, our finding that these two measures differed indicates that the COC features an extended outer matrix layer that is essentially free of cumulus cells—a novel and unexpected feature that, to our knowledge, has not been described previously. Specifically, we defined the mechanical height, H_{mech}, as the distance between the points of contact on the COC and the glass surface, which we determined from the combined motion of the AFM's z piezo and stepper motor to an accuracy of ~10 μm. The optical height, H_{opt}, on the other hand, was determined as the objective travel required to move the optical focus from the glass substrate to the outermost cumulus cells (multiplied by $n_{\mathrm{liquid}}/n_{\mathrm{air}} = 1.334$, to correct for the effect of the refractive index change between aqueous solution and air on the focusing). We estimate a resolution of 30 μm for this parameter, based on the accuracy of the focusing itself and the manual readout of the focus travel position. This is much less than the dimensions of the COC and thus provided measurements with good accuracy.

Fig. 4 *A* shows that the part of the matrix containing the oocyte and the cumulus cells is ~200 μm thick, independently of the method used for matrix expansion. Remarkably, the optically invisible cell-free coat contributes appreciably to the total coat extension. For in vivo expanded matrix, it adds another 200 μm to the total thickness. For in vitro expansion, the cell-free coat remains appreciable but its thickness reduces by 50%, indicating that factors in the follicle that are not present in vitro might play an important role in the formation of this part of the matrix.

To map the dimensions of the COC matrix laterally, H_{mech} and H_{opt} were measured as a function of the distance from the oocyte center. These results are also shown in Fig. 4 *A* and summarized in Fig. 4 *B*, in which the results of the correlative analysis of micromechanical and optical data are reflected in schemes that depict the extensions of the cumulus-containing and cumulus-free parts of matrix, the oocyte, and the cumulus cells drawn to scale. The sharp

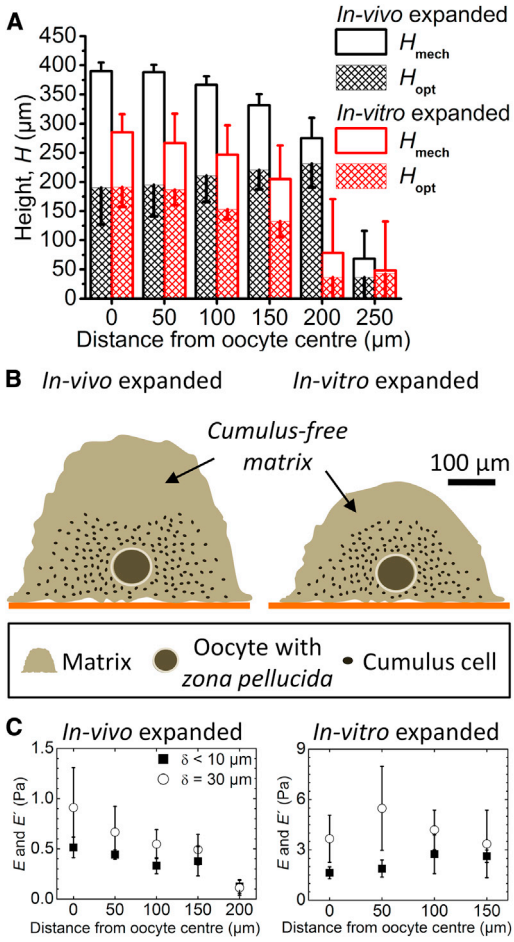

FIGURE 4 Determination of COC dimensions. (*A*) Heights, H_{mech} (determined mechanically from the contact point) and H_{opt} (determined optically from the location of the topmost cumulus cells), as a function of the distance from the oocyte center. Data represent the mean and standard deviations from measurements on three COCs; error bars are drawn along one direction only to facilitate visualization. (*B*) Illustration of the approximate dimensions of the COC matrix and the location of cumulus cells within it, as determined from the spatial mapping of H_{mech} and H_{opt}. The height of the oocyte above the substrate was determined optically. Oocyte and cumulus cell sizes are drawn to scale. (*C*) Elasticity of COCs expanded in vivo (*left*) and in vitro (*right*) as a function of distance from the oocyte center. Young's moduli in the linear elastic regime (*solid squares*) were determined through a fit with Eq. 1 for $\delta < 10$ μm; elastic moduli at $\delta = 30$ μm (*open circles*) were calculated with Eq. 2. Data represent the mean ± standard deviation from measurements on three individual COCs, except at 200 μm where only two of three in vivo expanded COCs had a matrix and were analyzed. To see this figure in color, go online.

drops in H_{mech} and H_{opt} between 200 and 250 μm distances for in vivo expanded matrix, and between 150 and 200 μm distances for in vitro expanded matrix, indicate that the lateral extension of the coat is not diffuse but is clearly delimited, and that the cell-free coat lining the immobilized COC matrix laterally is very thin. Moreover, we found no significant cumulus-free layer separating the substrate from the cumulus-containing matrix. At first, the asymmetric distribution of the cell-free coat (thick on the substrate-distal face, thin on the sides, and virtually absent on the substrate-proximal face of the COC) was surprising, as we expected the unperturbed COC matrix to have roughly spherical symmetry. We reasoned that COC immobilization somehow entails deformation of the cumulus-free matrix in the vicinity of the substrate. Apparently, the multivalent binding between HA in the matrix and CD44 on the substrate (Fig. 1 *A*, *inset*), possibly in conjunction with the gravitational forces exerted by the COC as a whole, is sufficiently strong to promote collapse of the extremely soft substrate-proximal matrix. We also noticed that H_{opt} measured across the oocyte (200 μm) was smaller than the lateral extension of the cumulus-containing matrix (400–500 μm for in vivo expanded matrix, and 300–400 μm for in vitro expanded matrix), and that the lateral diameter of the zona pellucida in immobilized COCs (~110 μm; Fig. 1 *B*, *left*) was larger than what is typically observed in free-floating COCs (~80 μm (42)). This suggests that immobilization also deforms the cumulus-containing part of the matrix as well as the oocyte-surrounding zona pellucida, though only moderately and to a much lesser extent than the cumulus-free substrate-proximal parts. On the other hand, the thickness of the cumulus-free substrate-distal part of the matrix (indicated by the length of the *open bars* in Fig. 4 *A*) was essentially constant within 150 μm from the oocyte center for in vitro expanded matrices and within 100 μm for in vivo expanded matrices, suggesting that this part of the matrix is largely unperturbed by the immobilization, although its apparent thickness could possibly be modified slightly by lateral matrix stretching upon immobilization or by gravity acting on the cells.

To test the homogeneity of the COC matrix, we analyzed force curves taken between 0 and 150 μm from the oocyte center (as well as 200 μm for in vivo expanded matrix), i.e., distances at which a matrix was clearly present (Fig. 4 *A*), at a selected loading rate (20 μm/s). Fig. 4 *C* shows that both the Young's modulus in the linear elastic regime ($\delta < 10$ μm; *solid squares*) and the effective modulus in the nonlinear elastic regime at a selected indentation ($\delta = 30$ μm; *open circles*) are virtually constant across the COC matrix, for matrices expanded in vivo as well as in vitro. This suggests that the matrix is homogeneous and that the presumably stiffer oocyte does not affect the measurements appreciably, consistent with expectations (43) based on the small indentation depths used compared with the total matrix thickness (<20%). The decrease in E and E' at 200 μm for in vivo expanded matrix (Fig. 4 *C*, *left*) appears to be an outlier. Fig. 4 *A* shows that the COC thickness decreases rapidly beyond 200 μm from the oocyte center. The measurements at the COC periphery are thus most likely performed on a strongly tilted COC-solution interface, and we propose that this effectively reduces the elastic modulus.

DISCUSSION

We have determined that the most compliant parts of the mouse COC matrix have a Young's modulus below 1 Pa, and the effective elastic modulus remains at a level of a few pascals across the range of strains tested (up to ~10%; Fig. 3). Considering all of the possible systematic errors described above, we estimate that the modulus values are accurate to within a factor of 2. To our knowledge, this is the lowest elastic modulus thus far determined for any mammalian tissue (44). By comparison, the Young's modulus for brain, which is typically considered one of the softest tissues, is ~2 orders of magnitudes higher than that observed for the COC matrix (45). The HA-rich glycocalyx lining the blood vessel endothelium is also considered very soft, and a Young's modulus in the range of a few 100 Pa has been reported for bovine lung microvascular endothelial cells (46). Within the larger animal kingdom, even the mostly acellular mesoglea of jellyfish exhibits local elastic modulus values that range between a few 10 Pa and a few 100 Pa (21). Furthermore, as reported by Velegol and Lanni (47), collagen gels formed in vitro at 0.5 mg/mL are predominantly elastic, with local elastic modulus values in the range of 1 Pa. We found that films reconstituted from HA and the matrix proteoglycan aggrecan (at 4 mg/mL total concentration) exhibited a Young's modulus of a few 10 Pa (29), and others reported predominantly elastic macroscopic hydrogels containing chemically cross-linked HA with Young's modulus values below 100 Pa (48–50), thus demonstrating that materials reconstituted from matrix molecules can also be very soft. Taken together, these comparisons illustrate that the COC matrix is extremely soft, and most likely is the predominantly elastic biological material with the lowest elastic modulus known to date.

To our knowledge, only a single study has hitherto reported a quantitative analysis of COC elasticity. Dunn and Picologlou (18) stretched entire COCs by 15–400% of the extension at rest and found a linear elastic response over the entire stretching range, with a Young's modulus of 150 Pa. In marked contrast, the value for Young's modulus that we report here is 2–3 orders of magnitude smaller, and our data show that the COC matrix stiffens appreciably even at a few percent compression (Fig. 3). This discrepancy suggests that the two measurements provide distinct information about COC matrix mechanics. On one hand, our AFM-based micromechanical method is particularly sensitive to the cumulus-free, soft outer shell of the COC. In the macromechanical approach of Dunn and Picologlou, on the other hand, the deformation of the inner and more rigid cumulus-containing part is monitored and the cumulus-free shell is largely neglected. The two methods thus are complementary and provide information about distinct parts of the COC matrix. We note that Dunn and Picologlou studied rabbit COCs that were expanded in vivo but extracted before ovulation, whereas our COCs were isolated from mice and were either expanded in vivo and extracted after ovulation or expanded in vitro. Differences in the animal sources and COC preparations used may also contribute to the distinct results observed by us and others. Future studies combining our micromechanical testing with frozen-cut COC sections should reveal valuable details about the mechanical heterogeneity of the COC matrix and the micromechanics of the inner parts of the COC matrix.

Previous studies have suggested that the COC matrix is a mesh-like network (51), that is, effectively a cross-linked hydrogel. Here, we found that even the softest and peripheral parts of the COC matrix are predominantly elastic (Fig. 2). This extends previous findings and indicates that the COC matrix is stably cross-linked throughout. It was previously demonstrated that HA together with the proteins TSG-6 (5) and pentraxin 3 (PTX3) (4), as well as the proteoglycan inter-α-inhibitor (IαI) (3,7), are essential for stabilization of the COC matrix and are sufficient to form a cross-linked hydrogel (6). The exact molecular nature of the cross-links, however, remains unknown. The elasticity of the COC matrix in our assays reveals that the cross-links are sufficiently stable to resist breakage on the timescale of seconds and minutes. The measured Young's modulus can provide a first estimate of the mesh size of the COC matrix. Specifically, for a homogeneous polymer meshwork that is dominated by cross-links, the so-called correlation length ξ (a statistical measure of the distance between segments on neighboring chains, or the effective mesh size) can be extracted approximately from $G \approx kT/\xi^3$, where G represents the so-called plateau shear modulus, and $kT = 4.1 \times 10^{-21}$ J is the thermal energy (52). From $E = 2G(1+\mu)$ and $E < 1$ Pa, we can estimate that the effective mesh size is on the order of a few hundred nanometers, i.e., the softest parts of the COC matrix are likely to be very sparsely cross-linked. This value is comparable to the correlation length reported for the chondrocyte pericellular matrix (PCM) based on optical force probe and particle exclusion assays (22). The PCM, like the COC matrix, is rich in HA. However, the PCM's overall topology must be distinct from the COC matrix because its mechanical stability is provided not by cross-links but by the tethering of long HA chains to the cell wall (22).

Interestingly, the mechanical response of in vitro expanded COCs contains an appreciable viscous contribution at low (<5 μm/s), but not high (>5 μm/s), approach speeds (Fig. 2 *C*). The drainage of liquid through the hydrogel pores during compression is a possible source of viscosity. Can poroelasticity explain our experimental observation? In a scaling approximation, the timescale associated with the liquid movement (the poroelastic time) is $t_p \approx L^2/D_p$, where L is the length scale associated with the indentation ($L^2 \approx R\delta$ for a spherical indenter (53)) and D_p is the poroelastic diffusion constant ($D_p \approx E_d\xi^2/\eta$, where E_d is the drained elastic modulus of the

hydrogel matrix and η is the viscosity of the draining solution) (54). With the above scaling approximation for the correlation length ξ and $E_d = 2G_d(1 + \mu)$, this gives $t_p \approx R\delta\eta/\{E_d^{1/3}[2kT(1 + \mu)]^{2/3}\}$. The drained elastic modulus is a lower limit of the measured value of Young's modulus ($E_d \leq E < 1$ Pa), and with $\eta \geq \eta_{water} \approx 1$ mPa·s and $\mu \leq 0.5$, we find $t_p \gtrsim 0.8\ s \times \delta/\mu m$. For comparison, the experimental compression time is $t_c \approx \delta/v_c$. Thus, $t_p/t_c \gtrsim 0.8$ at the lowest approach speed ($v_c = 1\ \mu$m/s), indicating that t_p and t_c may well be comparable and that the appreciable viscous responses at lower speeds arise from liquid drainage through the COC matrix. At the highest speed (20 μm/s), however, t_p is much larger than t_c, such that draining becomes negligible. The values of Young's modulus determined at higher speeds, therefore, represent the elasticity of the undrained matrix.

The clear segregation into a cumulus-cell-containing inner part and a cumulus-cell-free outer shell (Fig. 4), as well as its marked stiffening in response to stress (Fig. 3), indicates that the COC matrix is not a homogeneous structure. Specifically, the mechanical properties of the COC matrix suggest a heterogeneous network structure in which the mesh size increases with distance from the oocyte perimeter. Future studies in which the permeability of the COC matrix will be measured directly with probes of different sizes should be useful for defining the sieving properties and the fine structure of the COC matrix in more detail. In particular, it will be interesting to test whether the COC matrix exhibits a gradient of mesh size distribution similar to what was reported for the chondrocyte PCM (22), despite the distinct topologies of these two HA meshworks.

What are the functional implications of the COC matrix's mechanical properties and ultrastructure? An essential step in the reproductive process is the transport of the ovulated COC along the ciliated oviduct, and pickup and transport of the COC are tightly regulated by an interplay of mechanical and adhesive cues (17). It is clear that the COC matrix, and in particular the outer cumulus-cell-free layer, is extremely deformable. Matrix size and shape can vary in a large range upon applied force, but the original shape is fully restored once the mechanical perturbation is released (Fig. 2, *A* and *B*). This should ensure the structural and functional integrity of the COC throughout its transport through the narrow oviduct. Moreover, the large size and extreme softness of the COC matrix's outer shell may be crucial ingredients for its efficient capture and subsequent transport by the beating cilia that line the oviduct. Additionally, it is becoming increasingly apparent that biological hydrogels function as selective diffusion barriers, such that both the physical constraints imposed by the hydrogel's mesh size and specific interactions with the hydrogel's scaffold regulate macromolecular transport (55). In this regard, it is possible that the heterogeneity of the COC matrix provides spatiotemporal control over storage and access to signaling molecules and enzymes that are of critical importance for proper oocyte development and fertilization. Given the large mesh size of the HA matrix, physical constraints are probably of minor importance for the distribution of such proteins. However, signaling proteins are known to bind to matrix components such as the glycosaminoglycan chains on the proteoglycan versican, and heterogeneities in the biochemical environment may thus produce strong effects.

In this study, we have defined a thick and soft matrix coat surrounding the COC that is essentially free of cumulus cells (Fig. 4)—an unexpected feature that, to our knowledge, has not been reported previously. Remarkably, the coat is much less pronounced around in vitro expanded matrix, indicating that the in vivo environment provides unique cues that enable the formation of the cell-free coat. It is likely that antral granulosa cells, lining the antrum of the preovulatory follicle, contribute to this difference. Indeed, these cells produce HA, which likely becomes incorporated in the cumulus matrix (2). In addition, granulosa cells produce the proteoglycan versican, and versican binding to HA may well enhance the swelling of the outer coat (56). At this point, we can only speculate about the biological role of the cumulus-cell-free coat. Early in vitro work (57) indicated that sperm recognize the interfacial zone of the COC matrix and respond by changes in their orientation and in the beating pattern of their flagella. Moreover, a subpopulation of weakly motile sperm would not be capable of penetrating into the matrix. This raises the possibility that the additional coat discovered here is not only important for capture and transport of the ovum through the oviduct but also plays a role in the selection, capture, and guidance of sperm during fertilization. Clearly, there is a potential for comparative studies of sperm interactions with in vivo and in vitro expanded COCs to enhance our understanding of the initiation of sperm penetration and to improve the efficiency of in vitro fertilization procedures. Moreover, comparative micromechanical studies of in vivo and in vitro expanded COCs may help optimize oocyte in vitro maturation, a technique that is widely applied for the breeding of agriculturally important species and has been proposed as an alternative treatment in human-assisted reproduction technology to circumvent the drawbacks of standard ovarian-stimulation regimens (58).

CONCLUSIONS

We have successfully quantified the micromechanical response of the COC matrix to compression by colloidal-probe AFM. Owing to the nature of the COC matrix, it was necessary for us to develop a tailored immobilization procedure and to adapt the size of the colloidal probe. The matrix was confirmed to be elastic rather than plastic or viscous. The salient features of the COC compressive mechanics are an extreme degree of softness and a marked tendency to stiffen under stress. Through a combination of mechanical and optical analyses, we were able to identify

the presence of a thick cumulus-free coat that was particularly pronounced around in vivo expanded matrix. The heterogeneity of the COC matrix and the unique combination of elasticity and extreme softness may be functionally important, in particular for the maintenance of COC integrity during transport through the oviduct and for the proper selection, capture, and guidance of sperm. The methods we have established should also be valuable for characterizing HA-rich matrices in a wide range of other cells and tissues.

SUPPORTING MATERIAL

Two figures are available at http://www.biophysj.org/biophysj/supplemental/S0006-3495(16)30103-5.

AUTHOR CONTRIBUTIONS

X.C., A.S., and R.P.R. designed research. R.B. and A.S. prepared COCs. S.B. and D.G.J. prepared essential protein reagents. X.C. performed AFM experiments. X.C. and R.P.R. analyzed data and wrote the manuscript. All authors read and commented on the manuscript.

ACKNOWLEDGMENTS

We thank Luis Yate (CIC biomaGUNE) for the preparation of gold-coated glass coverslips, and Lionel Bureau (Laboratory of Interdisciplinary Physics) and Jessica Kwok (University of Leeds) for fruitful discussions.

This work was supported by the European Research Council Starting Grant JELLY (FP7-ERC-2012-StG-306435 to R.P.R.), the Spanish Ministry for Economy and Competitiveness (MAT2011-24306 to R.P.R.), and Unit Funding from the UK Medical Research Council (to D.G.J.).

SUPPORTING CITATIONS

References (31,38,41,59,60) appear in the Supporting Material.

REFERENCES

1. Russell, D. L., and A. Salustri. 2006. Extracellular matrix of the cumulus-oocyte complex. *Semin. Reprod. Med.* 24:217–227.
2. Salustri, A., M. Yanagishita, …, V. C. Hascall. 1992. Localization and synthesis of hyaluronic acid in the cumulus cells and mural granulosa cells of the preovulatory follicle. *Dev. Biol.* 151:541–551.
3. Chen, L., S. J. Mao, and W. J. Larsen. 1992. Identification of a factor in fetal bovine serum that stabilizes the cumulus extracellular matrix. A role for a member of the inter-alpha-trypsin inhibitor family. *J. Biol. Chem.* 267:12380–12386.
4. Salustri, A., C. Garlanda, …, A. Mantovani. 2004. PTX3 plays a key role in the organization of the cumulus oophorus extracellular matrix and in in vivo fertilization. *Development.* 131:1577–1586.
5. Fülöp, C., S. Szántó, …, K. Mikecz. 2003. Impaired cumulus mucification and female sterility in tumor necrosis factor-induced protein-6 deficient mice. *Development.* 130:2253–2261.
6. Baranova, N. S., A. Inforzato, …, R. P. Richter. 2014. Incorporation of pentraxin 3 into hyaluronan matrices is tightly regulated and promotes matrix cross-linking. *J. Biol. Chem.* 289:30481–30498.
7. Zhuo, L., M. Yoneda, …, K. Kimata. 2001. Defect in SHAP-hyaluronan complex causes severe female infertility. A study by inactivation of the bikunin gene in mice. *J. Biol. Chem.* 276:7693–7696.
8. Scarchilli, L., A. Camaioni, …, A. Salustri. 2007. PTX3 interacts with inter-alpha-trypsin inhibitor: implications for hyaluronan organization and cumulus oophorus expansion. *J. Biol. Chem.* 282:30161–30170.
9. Lam, X., C. Gieseke, …, P. Talbot. 2000. Assay and importance of adhesive interaction between hamster (Mesocricetus auratus) oocyte-cumulus complexes and the oviductal epithelium. *Biol. Reprod.* 62:579–588.
10. Eisenbach, M., and I. Tur-Kaspa. 1999. Do human eggs attract spermatozoa? *BioEssays.* 21:203–210.
11. Van Soom, A., S. Tanghe, …, A. de Kruif. 2002. Function of the cumulus oophorus before and during mammalian fertilization. *Reprod. Domest. Anim.* 37:144–151.
12. Hong, S. J., P. C. Chiu, …, W. S. B. Yeung. 2004. Establishment of a capillary-cumulus model to study the selection of sperm for fertilization by the cumulus oophorus. *Hum. Reprod.* 19:1562–1569.
13. Rienzi, L., G. Vajta, and F. Ubaldi. 2011. Predictive value of oocyte morphology in human IVF: a systematic review of the literature. *Hum. Reprod. Update.* 17:34–45.
14. Pathak, A., and S. Kumar. 2012. Independent regulation of tumor cell migration by matrix stiffness and confinement. *Proc. Natl. Acad. Sci. USA.* 109:10334–10339.
15. Engler, A. J., S. Sen, …, D. E. Discher. 2006. Matrix elasticity directs stem cell lineage specification. *Cell.* 126:677–689.
16. Paszek, M. J., N. Zahir, …, V. M. Weaver. 2005. Tensional homeostasis and the malignant phenotype. *Cancer Cell.* 8:241–254.
17. Talbot, P., C. Geiske, and M. Knoll. 1999. Oocyte pickup by the mammalian oviduct. *Mol. Biol. Cell.* 10:5–8.
18. Dunn, P. F., and B. F. Picologlou. 1976. Viscoelastic properties of cumulus oöphorus. *Biorheology.* 13:379–384.
19. Blandau, R. J., and J. L. Boling. 1973. An experimental approach to the study of egg transport through the oviducts of mammals. *In* Regulation of Mammalian Reproduction. S. J. Segal, R. Crozier, P. A. Corfman, and P. G. Condliffe, editors. Charles C. Thomas, Springfield, IL, pp. 400–415.
20. Boehm, H., T. A. Mundinger, …, J. E. Curtis. 2009. Mapping the mechanics and macromolecular organization of hyaluronan-rich cell coats. *Soft Matter.* 5:4331–4337.
21. Gambini, C., B. Abou, …, A. J. Cornelissen. 2012. Micro- and macrorheology of jellyfish extracellular matrix. *Biophys. J.* 102:1–9.
22. McLane, L. T., P. Chang, …, J. E. Curtis. 2013. Spatial organization and mechanical properties of the pericellular matrix on chondrocytes. *Biophys. J.* 104:986–996.
23. Stolz, M., R. Gottardi, …, U. Aebi. 2009. Early detection of aging cartilage and osteoarthritis in mice and patient samples using atomic force microscopy. *Nat. Nanotechnol.* 4:186–192.
24. Sokolov, I., S. Iyer, …, C. D. Woodworth. 2007. Detection of surface brush on biological cells in vitro with atomic force microscopy. *Appl. Phys. Lett.* 91:023902.
25. Ng, L., H. H. Hung, …, A. Grodzinsky. 2007. Nanomechanical properties of individual chondrocytes and their developing growth factor-stimulated pericellular matrix. *J. Biomech.* 40:1011–1023.
26. Lu, Y. B., K. Franze, …, A. Reichenbach. 2006. Viscoelastic properties of individual glial cells and neurons in the CNS. *Proc. Natl. Acad. Sci. USA.* 103:17759–17764.
27. Franze, K., M. Francke, …, J. Guck. 2011. Spatial mapping of the mechanical properties of the living retina using scanning force microscopy. *Soft Matter.* 7:3147–3154.
28. Staunton, J. R., B. L. Doss, …, R. Ros. 2016. Correlating confocal microscopy and atomic force indentation reveals metastatic cancer cells stiffen during invasion into collagen I matrices. *Sci. Rep.* 6:19686.
29. Attili, S., and R. P. Richter. 2013. Self-assembly and elasticity of hierarchical proteoglycan-hyaluronan brushes. *Soft Matter.* 9:10473–10483.

30. Guo, D., J. Li, …, J. Luo. 2014. Elastic properties of polystyrene nanospheres evaluated with atomic force microscopy: size effect and error analysis. *Langmuir.* 30:7206–7212.
31. Butt, H.-J., B. Cappella, and M. Kappl. 2005. Force measurements with the atomic force microscope: technique, interpretation and applications. *Surf. Sci. Rep.* 59:1–152.
32. Di Giacomo, M., A. Camaioni, …, A. Salustri. 2016. Cyclic AMP-elevating agents promote cumulus cell survival and hyaluronan matrix stability, thereby prolonging the time of mouse oocyte fertilizability. *J. Biol. Chem.* 291:3821–3836.
33. Naldini, L., U. Blömer, …, D. Trono. 1996. In vivo gene delivery and stable transduction of nondividing cells by a lentiviral vector. *Science.* 272:263–267.
34. Hutter, J. L., and J. Bechhoefer. 1993. Calibration of atomic-force microscope tips. *Rev. Sci. Instrum.* 64:1868–1873.
35. Baranova, N. S., E. Nilebäck, …, R. P. Richter. 2011. The inflammation-associated protein TSG-6 cross-links hyaluronan via hyaluronan-induced TSG-6 oligomers. *J. Biol. Chem.* 286:25675–25686.
36. Migliorini, E., D. Thakar, …, R. P. Richter. 2014. Well-defined biomimetic surfaces to characterize glycosaminoglycan-mediated interactions on the molecular, supramolecular and cellular levels. *Biomaterials.* 35:8903–8915.
37. Wolny, P. M., S. Banerji, …, R. P. Richter. 2010. Analysis of CD44-hyaluronan interactions in an artificial membrane system: insights into the distinct binding properties of high and low molecular weight hyaluronan. *J. Biol. Chem.* 285:30170–30180.
38. Hertz, H. 1881. Ueber die Berührung fester elastischer Körper. *J. Reine Angew. Math.* 92:156–171.
39. Poisson, S. D. 1827. Note sur l'extension des fils et des plaques élastiques. *Ann. Chimie. Phys.* 36:384–387.
40. Greaves, G. N., A. L. Greer, …, T. Rouxel. 2011. Poisson's ratio and modern materials. *Nat. Mater.* 10:823–837.
41. Sneddon, I. N. 1965. The relation between load and penetration in the axisymmetric Boussinesq problem for a punch of arbitrary profile. *Int. J. Eng. Sci.* 3:47–57.
42. Liu, C., E. S. Litscher, …, P. M. Wassarman. 1996. Targeted disruption of the mZP3 gene results in production of eggs lacking a zona pellucida and infertility in female mice. *Proc. Natl. Acad. Sci. USA.* 93:5431–5436.
43. Rico, F., P. Roca-Cusachs, …, D. Navajas. 2005. Probing mechanical properties of living cells by atomic force microscopy with blunted pyramidal cantilever tips. *Phys. Rev. E Stat. Nonlin. Soft Matter Phys.* 72:021914.
44. Levental, I., P. C. Georges, and P. A. Janmey. 2007. Soft biological materials and their impact on cell function. *Soft Matter.* 3:299–306.
45. Miller, K., K. Chinzei, …, P. Bednarz. 2000. Mechanical properties of brain tissue in-vivo: experiment and computer simulation. *J. Biomech.* 33:1369–1376.
46. O'Callaghan, R., K. M. Job, …, V. Hlady. 2011. Stiffness and heterogeneity of the pulmonary endothelial glycocalyx measured by atomic force microscopy. *Am. J. Physiol. Lung Cell. Mol. Physiol.* 301:L353–L360.
47. Velegol, D., and F. Lanni. 2001. Cell traction forces on soft biomaterials. I. Microrheology of type I collagen gels. *Biophys. J.* 81:1786–1792.
48. Ghosh, K., X. Z. Shu, …, R. A. F. Clark. 2005. Rheological characterization of in situ cross-linkable hyaluronan hydrogels. *Biomacromolecules.* 6:2857–2865.
49. Borzacchiello, A., L. Russo, …, L. Ambrosio. 2015. Hyaluronic acid based hydrogels for regenerative medicine applications. *BioMed Res. Int.* 2015:871218.
50. Vanderhooft, J. L., M. Alcoutlabi, …, G. D. Prestwich. 2009. Rheological properties of cross-linked hyaluronan-gelatin hydrogels for tissue engineering. *Macromol. Biosci.* 9:20–28.
51. Yudin, A. I., G. N. Cherr, and D. F. Katz. 1988. Structure of the cumulus matrix and zona pellucida in the golden hamster: a new view of sperm interaction with oocyte-associated extracellular matrices. *Cell Tissue Res.* 251:555–564.
52. Rubinstein, M., and R. H. Colby. 2003. Polymer Physics. Oxford University Press, Oxford/New York.
53. Hu, Y., X. Zhao, …, Z. Suo. 2010. Using indentation to characterize the poroelasticity of gels. *Appl. Phys. Lett.* 96:121904.
54. Moeendarbary, E., L. Valon, …, G. T. Charras. 2013. The cytoplasm of living cells behaves as a poroelastic material. *Nat. Mater.* 12:253–261.
55. Lieleg, O., and K. Ribbeck. 2011. Biological hydrogels as selective diffusion barriers. *Trends Cell Biol.* 21:543–551.
56. Dunning, K. R., M. Lane, …, D. L. Russell. 2007. Altered composition of the cumulus-oocyte complex matrix during in vitro maturation of oocytes. *Hum. Reprod.* 22:2842–2850.
57. Drobnis, E. Z., A. I. Yudin, …, D. F. Katz. 1988. Kinematics of hamster sperm during penetration of the cumulus cell matrix. *Gamete Res.* 21:367–383.
58. Coticchio, G., M. Dal-Canto, …, R. Fadini. 2012. Human oocyte maturation in vitro. *Int. J. Dev. Biol.* 56:909–918.
59. Cappella, B., and G. Dietler. 1999. Force-distance curves by atomic force microscopy. *Surf. Sci. Rep.* 34:1–3, 5–104.
60. Johnson, K. L., K. Kendall, and A. D. Roberts. 1971. Surface energy and the contact of elastic solids. *Proc. R. Soc. Lond. A Math. Phys. Sci.* 324:301–313.